PHYSICAL REVIEW B **79**, 205403 (2009)

Pattern evolution on previously rippled Au(001) by crossing-ion-beam sputtering

J.-H. Kim,[1] M. Joe,[2] S.-P. Kim,[3] N.-B. Ha,[1] K.-R. Lee,[3] B. Kahng,[2] and J.-S. Kim[1,*]
[1]*Department of Physics, Sook-Myung Women's University, Seoul 140-742, Korea*
[2]*Department of Physics and Astronomy, Seoul National University, Seoul 151-747, Korea*
[3]*Computational Science Center, Korea Institute of Science and Technology, Seoul 136-791, Korea*

(Received 15 December 2008; revised manuscript received 16 April 2009; published 6 May 2009)

We study the pattern evolution of pre-rippled Au(001) during sputtering by an ion beam that is incident perpendicular to the initial ripple in azimuth at a grazing angle. Prepatterned ripples decay exponentially with time and new ripples develop only after extended flat areas form along the crossing-ion beams. Hence, the superposition of the initial and new ripple patterns does not occur. The kinetic behaviors of new ripples growing on pre-rippled Au(001) by the crossing-ion beams are distinct from those on initially flat Au(001). When comparing the pre-rippled surface to the initially flat surface, the morphological evolution is substantially influenced by enhanced nonlinear effects such as redeposition.

DOI: 10.1103/PhysRevB.79.205403 PACS number(s): 81.16.Rf, 79.20.Rf

I. INTRODUCTION

Ion-beam sputtering has attracted considerable attention as an effective way of fabricating self-organized nanostructures on a wide range of materials, such as metals, insulators, and semiconductors, regardless of their crystallinity.[1] For instance, periodic ripple structures form on the surfaces of Si,[2,3] Ge,[4] glass,[5] graphite,[6] Ag,[7] Cu,[8,9] and polymers[10] by oblique ion-beam sputtering. On the other hand, nanodot patterns have been found to develop on surfaces of Si,[11] GaSb,[12] InP,[13] Pd,[14] and MgO (Ref. 15) when ion-beam sputtering is made approximately normal to the surface.

To understand the pattern evolution, many theoretical models with different levels of sophistication have been proposed. Bradley and Harper[16] (BH) proposed a linear continuum model by combining Sigmund's model of ion-beam erosion[17,18] with diffusion theory.[19,20] This model predicts the formation of periodic patterns as a consequence of the competition between roughening by the sputter erosion and smoothing by the surface diffusion of adatoms and vacancies. The BH model is successful in predicting the ripple formation and its orientation, but it fails to explain ripple stabilization and ripple coarsening. To compensate for those limitations, various models, such as the Kuramoto-Sivashinsky (KS) model[21] and its elaborate versions including the damped KS model,[22] extended KS model,[14] and hydrodynamic model,[23] have been introduced. Those models take various nonlinear effects into account and can explain some features that cannot be described by the BH model, such as ripple stabilization,[21] kinetic roughening,[14] and ripple coarsening.[23]

Most of the sputter-induced nanopatterns achieved so far are limited to hexagonal or square arrays of dots or holes and ripples on flat surfaces. The goal should be, however, to fabricate more diverse nanostructures in a predictable manner with improved control over the nanostructuring process or sculpting on a nanometer scale. Recently proposed is the fabrication of nanopatterns by multiple ion-beam sputtering, in which more than one ion beam is projected on a surface simultaneously.[24,25] Joe *et al.*[26] produced square-symmetric patterns of nanoholes and nanodots on Au(001) by dual ion-beam sputtering, where two perpendicular ion beams were incident on a substrate simultaneously. However, the application of the multiple ion-beam sputtering is limited by the chamber design and is thus generally not flexible. As an alternative, Vogel and Linz[25] proposed patterning through sequential ion-beam sputtering (SIBS) with varying sample orientations relative to an ion beam. However, to date, experimental realization of SIBS has not been reported.

In the present work, we examine the possibility of nanosculpting by SIBS with a simple model system: we form a ripple pattern on Au(001) by sputtering a sample at an oblique angle in one direction and then continue to sputter it after rotating the sample by 90° azimuthally while maintaining the same polar angle (Fig. 1). Although we perform this type of SIBS under various sputtering conditions, we find no superposition of the ripples formed by each ion-beam sputtering. This result contradicts previous theoretical predictions.[25]

The present work can also be viewed as a study on the morphological evolution of the prepatterned surface by ion-beam sputtering and offers a rare chance to examine theoretical models against salient experimental results. Indeed, due to the sloped and rough surface, nonlinear effects, such as slope-dependent erosion and redeposition, play more significant roles in morphological and pattern evolution for pre-rippled surface than for an initially flat surface.

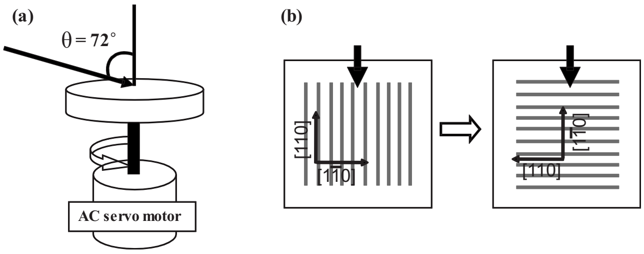

FIG. 1. (a) Schematic view of sputter geometry and rotatable substrate by the ac servomotor. (b) Schematic view of the CIBS. After the initial ripple formed (left), we rotated the sample such that it was perpendicular to the ion beam (right). Solid arrows signify the ion-beam directions.

TABLE I. The sputter conditions of the erosive and diffusive regimes

	Partial pressure of Ar, P_{Ar} (Torr)	Energy, ε (keV)	Flux, f ($\mathrm{nm}^{-2}\ \mathrm{s}^{-1}$)
The erosive regime	1.3×10^{-4}	2.0	0.3125
The diffusive regime	1.3×10^{-4}	0.5	0.0625

II. EXPERIMENT

Sample cleaning and sputtering experiments were performed in an ultrahigh vacuum chamber with a base pressure of 5×10^{-10} Torr. The sample was disk-shaped single crystalline Au(001) with a diameter of 1 cm. To fabricate the initial ripple, the in-plane direction of the incident ion beam was aligned along the densely packed [110] direction of the sample and then along $[1\bar{1}0]$ for the subsequent sputtering. The azimuthal angle of the sample was adjusted for SIBS by rotating it using an ac servomotor while keeping the polar angle θ at 72° from the surface normal [Fig. 1(a)].

Sputtering was performed in both the erosive and diffusive regimes.[27,28] In the erosive regime, the ripple formation was governed by ion-beam erosion and the resulting ripples were oriented along the ion-beam direction. In the diffusive regime, the diffusion of adatoms and vacancies controlled the pattern formation and ripples formed along the densely packed crystallographic directions The sputter conditions employed in the present experiments to reach the two different regimes are summarized in Table I.

During crossing-ion-beam sputtering (CIBS) of the prepatterned ripples, each sputter period was limited to 5 min, and thus, the maximal sputter-induced heating of the sample was maintained at less than 5 K. The ion fluence ψ for CIBS thus signifies the ion flux times the cumulative sum of the previous sputter times. The ion beam is highly collimated by an electric lens and the effects of beam divergence[11] should also be negligible.

The patterned surface was investigated *ex situ* by an atomic force microscope (AFM) operated in the contact mode. The surface roughness W was obtained from each image by $W\equiv[\frac{1}{N}\Sigma_{i=1}^{N}(h(x_i)-\bar{h})^2]^{1/2}$, where N is the number of pixels forming the image, $h(x_i)$ is the height at lattice site x_i, and $\bar{h}\equiv\frac{1}{N}\Sigma_{i=1}^{N}h(x_i)$ is the average height.

In the erosive regime, the mean wavelength of the initial ripple pattern, λ_I, was obtained from the two-dimensional height-height correlation function of the corresponding ripple pattern. In the diffusive regime, however, λ_I was not well defined by the height-height correlation function due to the frequent merging of the ripples. In this case, λ_I was estimated from line profiles across the ripples for numerous images.

During CIBS, the new ripples coexisted with the modified initial ripples. We took a line profile and separated the morphological information of one from the other. This procedure was repeated with many line profiles from numerous images; the mean amplitude A_N and the wavelength λ_N of the new ripples were thus determined.

III. RESULTS

Figure 2(a) shows the surface morphology after crossing-ion-beam sputtering of an initially flat Au(001) with $\psi=4500\ \mathrm{ions\ nm}^{-2}$ in the erosive regime, where λ_I and W of this initial ripple pattern are 28.7 and 1.95 nm, respectively. The ripples are aligned parallel to the ion-beam direction or [110] represented by a solid arrow in the figure. Most of the ripples are quite straight and extended beyond 3 μm, the maximal scan range of our AFM. The reason for the formation of such a highly ordered ripple pattern is the precise alignment of the incident-beam direction to the densely packed [110] crystallographic direction of the sample.

Figures 2(b)–2(d) illustrate the evolution of the initial ripple pattern in Fig. 2(a) by CIBS with an increase in the ion

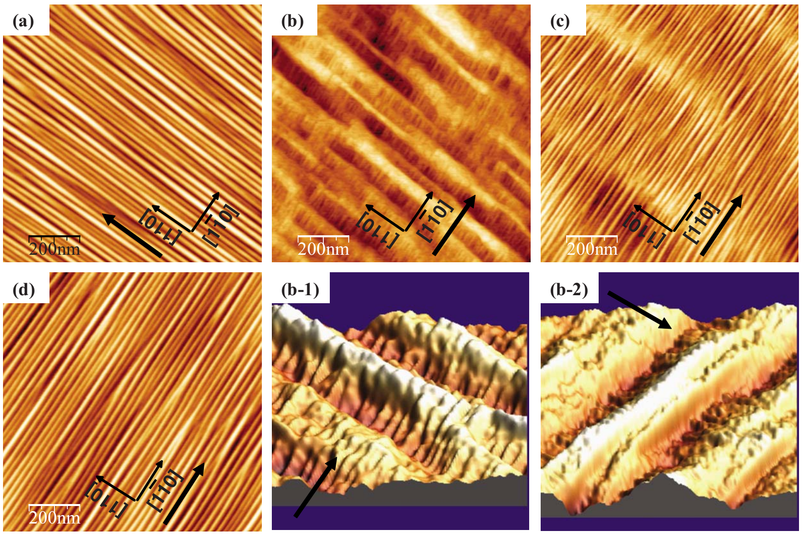

FIG. 2. (Color online) AFM images ($1\times1\ \mu\mathrm{m}^2$) of the surface after sputtering in the erosive regime. (a) Initial rippled surface generated by ion-beam sputtering. Surface morphology after CIBS at (b) $\psi=75.0\ \mathrm{ions\ nm}^{-2}$, (c) $\psi=468.8\ \mathrm{ions\ nm}^{-2}$, and (d) $\psi=1875.0\ \mathrm{ions\ nm}^{-2}$. (b-1) and (b-2) are three-dimensional detailed images ($457\times457\ \mathrm{nm}^2$) of a representative area in (b); (b-1) illuminated and (b-2) shadowed sides of the initial ripples. All the arrows within the figures indicate the ion-beam direction.

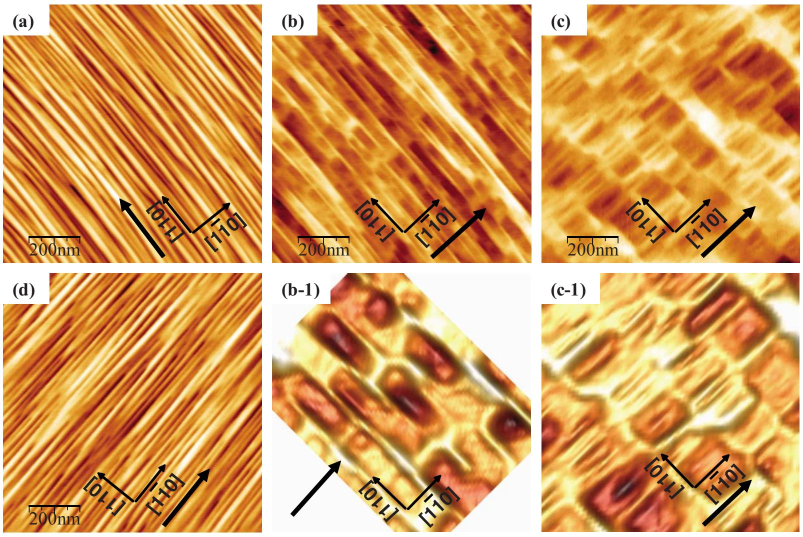

FIG. 3. (Color online) AFM images (1×1 μm^2) of surfaces after sputtering in the diffusive regime. (a) Initial rippled surface by ion-beam sputtering. Surface morphology after CIBS at (b) $\psi=153.8$ ions nm^{-2}, (c) $\psi=716.3$ ions nm^{-2}, and (d) $\psi=7128.8$ ions nm^{-2}. (b-1) and (c-1) are three-dimensional detailed images (318×238 nm^2, 560×540 nm^2); (b-1) is a representative rectangular pattern in (b), and (c-1) is a representative new ripple nested in a rectangular pattern in (c). All of the arrows in the figures denote the ion-beam direction.

fluence. In Fig. 2(b), the shape of the initial ripple pattern is drastically changed from a regular sinusoidal shape to an irregular one, even though the surface is exposed to a low ion fluence of $\psi=75.0$ ions nm^{-2}. The mean value of the ripple wavelengths dramatically increases to $\lambda_I\sim 100$ nm over a wide distribution ranging from 70 to 150 nm, while the coherence length of the ripple substantially decreases to less than 800 nm. Moreover, W of the initial ripple pattern decreases to 0.56 from 1.95 nm, indicating that the surface is now significantly smoother.

New ripples are already observed to develop along the direction of the crossing-ion beam in Fig. 2(b). The amplitude A_N and wavelength λ_N of the new ripple are about 0.14 and 17 nm, respectively. Note that they grow selectively on the illuminated side (by the ion beam) of initial ripples, as shown in detail in Fig. 2(b) and 1. On the shadowed side, however, no easily discernible ripple develops [Fig. 2(b) and 2]. The sputter yield on the shadowed side is smaller due to the higher sputter angle (from the surface normal) as compared to that on the illuminated side. Moreover, when comparing the flat area on the shadowed side to that on the illuminated side, it is too narrow for the new ripple to form without interruption. Thus, the development of the new ripple seems retarded on the shadowed side, as compared to that on the illuminated side.

With $\psi=468.8$ ions nm^{-2}, the initial ripples almost disappear [Fig. 2(c)]. Its mean amplitude A_I is smaller than 0.5 nm, while λ_I increases to 450 nm. In contrast, new ripples continue to grow. A_N and λ_N are 0.61 and 22 nm, respectively. The coherence length of the new ripple is longer than 450 nm and is limited merely by the remnants of the initial ripple.

With $\psi=1875.0$ ions nm^{-2}, the initial ripples disappear completely and only the new ripples are visible [Fig. 2(d)]. At the same time, the new ripple reaches a quasistationary state with a coherence length longer than 3 μm, $\lambda_N\approx 26$ nm, and $W\approx 1.14$ nm.

In order to investigate the effects of diffusion of adatoms and advacancies on pattern formation, CIBS was also performed in the diffusive regime. Figure 3(a) shows the initial ripple of the diffusive regime with $\psi=7200$ ions nm^{-2}. Each ripple is also oriented parallel to the ion-beam direction or [110] direction. W and λ_I are 2.03 and 29.9 nm, respectively, and are similar to the values observed for the initial ripple in the erosive regime.

In the diffusive regime, merging of the neighboring ripples occurs frequently, even though the ion-beam direction is well aligned along the [110] crystallographic direction. As a result, the coherence length of the ripple is less than 1 μm. Moreover, the distributions of both λ_I and A_I of the ripples are typically 20–50 and 0.5–4.1 nm, respectively [Fig. 3(a)], whereas those of λ_I and A_I in the erosive regime are much narrower, 17–32 and 0.9–2.6 nm, respectively. [Fig. 2(a)]. In the diffusive regime, diffusion of adatoms between neighboring ripples frequently leads to the interruption of the long-range order of the ripple pattern, a phenomenon that is rarely observed in the erosive regime.

The evolution of the ripple pattern by CIBS in the diffusive regime is illustrated in Figs. 3(b)–3(d) with increasing fluence. For $\psi=153.8$ ions nm^{-2}, W decreases to 1.13 nm and λ_I increases to 52 nm [Fig. 3(b)]. Interestingly, we observe ridges that bridge adjacent initial ripples. Figure 3(b) and 1 shows a detailed three-dimensional view of a representative bridging structure in Fig. 3(b). The distance between bridging structures has a wide distribution, from 50 to 130 nm. The mean distance between bridging structures is very large compared to the mean wavelength $\lambda_N=27$ nm of the new ripple that develops in the later stages due to subsequent sputtering [Fig. 3(d)]. The initial ripples and the bridging structures combine to form rectangular patterns of various sizes that are not observed in the erosive regime.

When ψ reaches 716.3 ions nm^{-2}, W decreases to 6.8 nm while λ_I notably increases to approximately 150 nm [Fig. 3(c)]. At the same time, the rectangular pattern enlarges and, therein, new ripples nest densely with λ_N from 20 to 40 nm and A_N varying from 0.2 to 1.0 nm [Fig. 3(c) and 1]. The coherence length of the nested ripples is limited by the boundary of the rectangular structure.

Continued sputtering results in the disappearance of the initial ripple and the new ripples prevail over the surface [Fig. 3(d)]. This ripple pattern is characterized by $\lambda_N\approx 27$ nm and $W\approx 0.8$ nm. λ_N and W do not change with

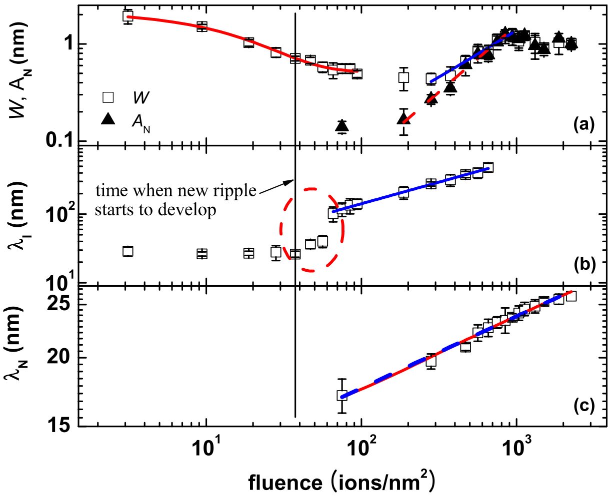

FIG. 4. (Color online) Evolution of surface morphology by ion-beam sputtering in the erosive regime. (a) Surface roughness W and new ripple amplitude A_N vs ion fluence. Solid red line (on left-hand side) represents an exponential fit to W during its decay and solid blue line (on the right-hand side) represents a power-law fit to W during its growth, with growth exponent $\beta=0.96\pm0.09$. Dashed red line corresponds to a power-law fit to A_N with $\beta=1.38\pm0.12$. (b) Wavelength of the initial ripple λ_I vs ion fluence. Solid blue line denotes a power-law fit with coarsening exponent $n=0.63\pm0.09$. (c) Wavelength of the new ripple λ_N vs ion fluence. Solid red line denotes a logarithmic fit and dashed blue line denotes a power-law fit with coarsening exponent $n=0.13\pm0.01$.

further increase of ion fluence, signaling that steady state is reached.

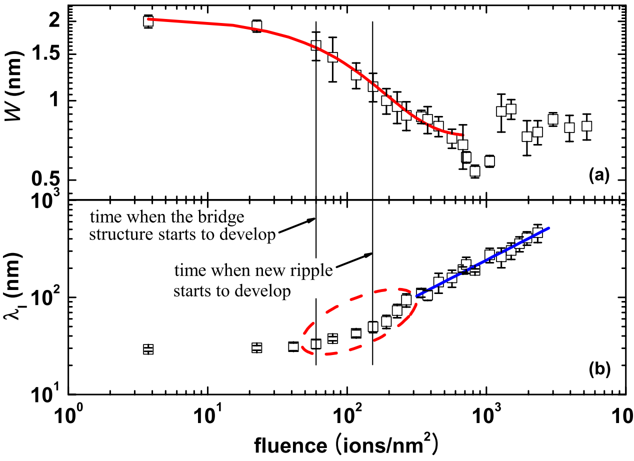

FIG. 5. (Color online) Evolution of surface morphology by ion-beam sputtering in the diffusive regime. (a) Roughness W vs ion fluence. Solid red line in the decay portion denotes an exponential fit to W. (b) Wavelength of the initial ripple λ_I vs ion fluence. Solid blue line denotes a power-law fit to λ_I with a coarsening exponent $n=0.74\pm0.04$.

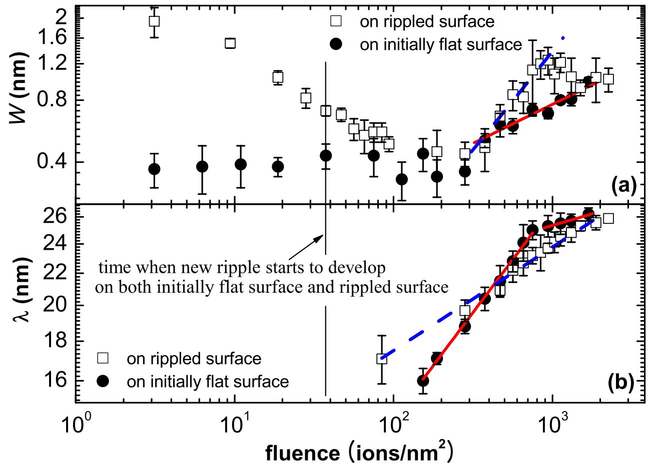

FIG. 6. (Color online) Comparison of the morphological evolution from the initially flat surface (filled circle) when ion-beam sputtering is performed in the erosive regime to that from the prepatterned surface (empty square). (a) Roughness W vs ion fluence. Solid red line (dotted blue line) denotes a power-law fit to W of the initially flat surface [the prepatterned surface, as previously noted in Fig. 4(a)] with a growth exponent $\beta=0.38\pm0.04$ ($\beta=0.96\pm0.09$). (b) New ripple wavelength λ vs ion fluence. Solid red line (dotted blue line) denotes a power-law fit to λ of the initially flat surface [prepatterned surface, as previously noted in Fig. 4(c)] with a coarsening exponent $n=0.30\pm0.01$ before the crossover and then $n=0.06\pm0.01$ ($n=0.13\pm0.01$).

We summarize the evolution of surface roughness W and ripple wavelength λ during CIBS in both the erosive and diffusive regimes in Figs. 4 and 5. Figure 4(a) shows W as a function of ion fluence in the erosive regime. In the early stages, W decreases exponentially and reaches its minimum at approximately $\psi=281$ ions nm^{-2}, indicating very efficient smoothing by CIBS. Note that the new ripple starts to develop around $\psi=37.5$ ions nm^{-2}, before W is minimized, thus increasing W again at a high growth rate. A power-law fit to W requires a large growth exponent β of 0.96 ± 0.09.[29] An exponential fit to W also works well, with a χ^2 of 0.5092, slightly higher than that for the power-law fit, 0.4223.[30] Furthermore, β reflects both the growth of a new ripple and the decay of the initial ripple. To isolate the mean amplitude of the new ripple A_N, we subtract the contribution of the initial ripple from each line profile obtained from the images, as shown in Fig. 2. A_N follows the power law with a larger β ~1.38 than that of W [Fig. 4(a)]. This β is very large compared to $\beta\sim0.38$ obtained for the initially flat surface under the same sputtering conditions [Fig. 6(a)], indicating that the growth kinetics of the new ripples on the pre-rippled surface is quite different from that on the initially flat surface. Moreover, no model predicts the high $\beta\geq1$ observed during the growth of the new ripple.[29]

λ_I is almost constant in the early stages of CIBS or before ψ reaches 37.5 ions nm^{-2} [Fig. 4(b)]. However, λ_I abruptly increases between $\psi=37.5$ ions nm^{-2} and $\psi=65.6$ ions nm^{-2} [the dotted region in Fig. 4(b)] and then follows a power law with a coarsening exponent $n=0.63\pm0.09$. The start of the transition period coincides with the start of the new ripple development.

The temporal evolution of λ_N in the erosive regime is shown in Fig. 4(c). The dashed blue line represents a power-law fit $\lambda_N\sim t^n$ with a coarsening exponent $n=0.13\pm0.01$; that value is very small in comparison to the values predicted by various models.[29] Thus, we also fit the experimental results with the logarithmic function (solid red line), which gives $\chi^2=0.1081$; this value is slightly smaller than that for the power-law fit of $\chi^2=0.1120$. Such ripple coarsening is, however, incompatible with the prediction of the BH and KS models.

Figure 5 shows the temporal evolution of both W and λ_I in the diffusive regime. In Fig. 5(a), W decays exponentially in the early stages of CIBS, similar in behavior to the erosive regime. With increasing fluence, new ripples develop and W starts to increase again. Since W or A_N reaches a stationary state within a decade, their scaling behavior is not well established. In Fig. 5(b), λ_I is almost constant until $\psi=60.0$ ions nm^{-2}, but then it starts to increase (the red dotted region). After this transition period, λ_I increases, following a power-law behavior with a large $n=0.74\pm0.04$, as was the case for the erosive regime in Fig. 4(b). Compared to the erosive regime, however, the transition period is longer and the change in λ_I during that period is not as abrupt. Actually, λ_I has two subperiods within the transition period: a slow increase in the beginning followed by rapid growth. The onset of each subperiod is accompanied, respectively, by the development of a bridging structure ($\psi=60.0$ ions nm^{-2}) and of a new ripple ($\psi=153.8$ ions nm^{-2}). In the diffusive regime, the new ripples coexist with the bridging structures and frequently merge with neighboring ones. Thus, a well-defined λ_N cannot be obtained over an extended period and will not be discussed further.

To compare the morphological evolution of the pre-rippled surface to that of the initially flat Au(001), we performed ion bean sputtering on the initially flat surface under the same experimental conditions as those used in the erosive regime. Under these conditions, we also observed the development of a ripple structure parallel to the ion-beam direction (figure not shown). Figure 6(a) summarizes the comparison between the temporal evolution of the roughness of the ripples formed on the flat surface, W_F, and that on the pre-rippled surface. W_F remains almost constant until $\psi=281.3$ ions nm^{-2}, fluctuating around an initial roughness, 0.37 nm. After the incipient stage, W_F increases, closely following the power law with $\beta=0.38\pm0.04$. It is much smaller than that observed during CIBS.

The coarsening of the ripple wavelength λ_F is summarized in Fig. 6(b). The coarsening exponent shows a crossover from $n=0.3$ to 0.06. We note that such behavior is in sharp contrast to that on the pre-rippled surface in the erosive regime, in which coarsening of the new ripple follows the power law with $n=0.13$ or logarithmic behavior. This result implies that during sputtering, the growth kinetics of ripples on the initially flat surface is different from that on the pre-rippled surface.

IV. DISCUSSION

A. Sputter-induced smoothing

Exponential decay of W is observed in the early stages of CIBS in both the erosive and diffusive regimes, as shown in Figs. 4(a) and 5(a), respectively. Similar sputter-induced smoothing is also found in previous studies. Fan *et al.*[31] studied the morphological evolution of Si nanodots by ion-beam sputtering and also observed the exponential decay of the dot heights. The numerical integration of the KS equation was used to elucidate the observed morphological evolution, but did not yield satisfying results. However, the temporal evolution of the nanodot pattern[31] and its dependence on the incident ion flux[32] could be better described by adding a damping term, $-\alpha h$, to the KS equation, known as the damped KS equation (dKS).[22] The damping term is partly attributed to the redeposition of sputtered atoms.

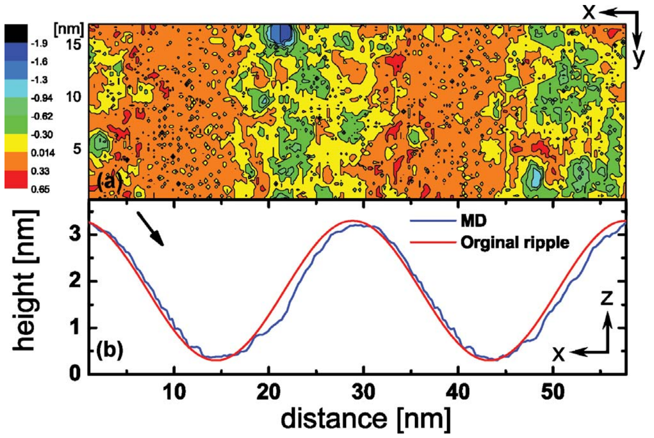

FIG. 7. (Color online) Surface profiles after being sputtered by 0.96 ions nm^{-2} of Ar$^+$ across the ripples with an incidence energy of 2.0 keV. (a) Plot of the height difference after sputtering. Negative values denote erosion, while positive values denote an increase of the surface height due to redeposition. (b) Profiles of the rippled surface before and after sputtering. Profiles of the ripples after sputtering are obtained from (a) after averaging along the direction of each ripple or perpendicular to the train of ripples. Arrow in (b) denotes the direction of the incident ion beam.

In line with the above argument, Toyoda *et al.*[33] observed that initially rippled surface underwent exponential decay of its roughness by cluster-ion-beam sputtering. They introduced a model in which some of the sputtered atoms redeposited, diffused toward the bottom of the valleys, and then filled them. This picture was supported by their kinetic Monte Carlo (MC) simulations. The researches of both Fan *et al.*[31] and Toyoda *et al.*[33] suggest that redeposition of sputtered atoms plays a significant role in the sputter-induced smoothing of the present pre-rippled surface.

To examine this picture more concretely, we performed a classical molecular-dynamics (MD) simulation of CIBS on a pre-rippled surface modeled after a sinusoidal wave with the same mean amplitude and wavelength as those observed in Fig. 2(a). We used the embedded atom method (EAM) potential for Au (Ref. 34) and the Ziegler, Biersack, and Littmark (ZBL) potential[35] to describe the highly repulsive behavior at a short distance. Utilizing the switching function, the pairwise potential in EAM was modified to smoothly join the ZBL potential within 0.2 of the atomic distance, thus avoiding splining errors and the derivative discontinuity problem.[36,37] With this method, the sputter erosion and redeposition were rigorously treated, although the thermal diffusion of redeposited adatoms was not fully taken into account.

Figure 7(a) shows a map of the height change after sputtering the initial sinusoidal ripple. Although the total fluence is limited to $\psi = 0.96$ ions nm^{-2} due to computational limitations, we clearly observe the morphology variation. Along with the initial ripples, Fig. 7(b) shows the height profiles of the sputtered ripples after averaging along each ripple. The height of the sputtered ripple on the illuminated side and near its top decreases due to sputter erosion. Note that the redeposition substantially contributes to the morphological evolution. The height of the shadowed side significantly increases due to the redeposition. Some of the sputtered atoms also land on the valley and slightly increases the valley height. Overall, the mean amplitude of the ripple decreases and the rippled surface eventually is smoothed by sputter erosion and redeposition. If the diffusions of the redeposited atoms are taken into account, smoothing of the rippled surface would be further expedited. These results support the model of Toyoda *et al.*[33] and the observations of Fan *et al.*[31] that indicate the significance of redeposition, but contradict the BH theory that predicts the instability caused by sputter erosion.[16]

B. Coarsening of the initial ripple

Figures 4(b) and 5(b) show the evolution of λ_I in both the erosive and diffusive regimes, respectively. λ_I is constant in the early sputtering stages in both regimes. In the erosive regime, λ_I shows an abrupt increase when the new ripples develop. [See the transition region indicated by the dotted red ellipse in Fig. 4(b).]

In the diffusive regime, however, the coarsening of the initial ripples starts before the new ripples develop (Fig. 5). A key difference from the erosive regime is the formation of structures bridging neighboring initial ripples before new ripples develop [Figs. 3(b), 3(b), and 1]. These bridges can play the same role as new ripples do. In Fig. 5, the coarsening rate during the bridge forming stage is, however, lower than that during the ripple forming stage. It may originate from the fact that the density of the bridge structure is lower than that of the new ripples.

The coincidence of the onset of coarsening of the initial ripple with the development of the structures connecting the adjacent ripples suggests that the new ripples and the bridging structures play significant roles in the coarsening of the initial ripples. Actually, before the new ripples or the bridging structures develop, each initial ripple is isolated and little coarsening of the initial ripple is observed. The step edges of the new ripples and bridging structures are oriented in the close-packed [110] direction and the diffusion barrier encountered by adatoms along the edge is very low. It means that the bridging structures can offer very efficient channels mediating mass transport between adjacent initial ripples. If the two neighboring ripples have different sizes or shapes that give rise to different vapor pressures of adatoms, then there may be net mass flow between the two ripples. As a result, ripening of one ripple may occur at the expense of the other, thus increasing λ_I. This conjecture for the ripple-mediated ripening is, however, awaited to be further examined by the independent studies such as kinetic Monte Carlo simulations.

After the transition periods, λ_I increases with the coarsening exponent n of 0.63 and 0.74 for the erosive and the diffusive regimes, respectively. On the other hand, n for the thermal coarsening of mounds is usually less than 0.5.[38–40] The coarsening exponents observed in the present experiments are distinctly higher than those observed during the thermal coarsening of mounds. This observation suggests that the coarsening of the initial ripples proceeds via mechanisms different from those for the mound coarsening, possibly via the aforementioned ripple-mediated diffusion along its step edges that is a characteristic of the pre-rippled surface but is not available in the usual two-dimensional coarsening of the mounds.

C. Kinetic behaviors on the pre-rippled surface versus those on the initially flat surface

During CIBS, W increases after reaching its minimum as the new ripples develop (Figs. 4 and 5). In the erosive regime [Fig. 4(a)], W follows the power law with a growth exponent $\beta = 0.96 \pm 0.09$. This is much higher than the $\beta = 0.38$ observed for an initially flat Au(001) under the same sputtering conditions for CIBS [Fig. 6(a)]. Note that there are some differences between the two cases. On the pre-rippled surface, new ripples develop preferentially on the extended flat area of the illuminated side of the initial ripples in the early stages [Figs. 2(b), 2(b), and 1]. Thus, the local incidence angle of the ion beam, θ [Fig. 1(a)], is smaller for the pre-rippled surface than for flat surface. Consequently, the sputter yield is larger on the pre-rippled surface than on the flat surface. This, in turn, gives rise to a morphological evolution or growth exponent for the pre-rippled surface that differs from that for the flat surface.

During CIBS in the erosive regime, λ_N of the new ripples follows a logarithmic behavior, represented by the solid (red) line in Fig. 4(c), or a power law with a very low coarsening exponent, $n = 0.13 \pm 0.01$, represented by a dashed (blue) line in Fig. 4(c). On the initially flat surface, λ_F follows a power law with $n \sim 0.3$ in the early stages. In the later stages, however, the surface becomes as rough as the pre-rippled surface and shows coarsening behavior with small $n \sim 0.06$ or logarithmic behavior similar to the pre-rippled surface [Fig. 6(b)]. The crossover behavior in the ripple coarsening on the initially flat surface seems to be triggered by the roughening of the initially flat surface by the continued sputtering.

Similar crossover behavior was previously observed.[41] As sputtering proceeded, W of an initially flat Pd(001) showed a crossover from a power-law behavior to a logarithmic behavior in the later stages.[41] The crossover behavior was attributed to the enhanced probability of redeposition because the capture angle of the sputtered atoms increased for the roughened surface. In this picture, the difference in the coarsening behavior between the pre-rippled surface and the initially flat surface can be understood in the following manner: for the pre-rippled surface, W is rough from the beginning and the redeposition is already significant, showing weak variation of morphology or the logarithmic dependence of λ. For the initially flat surface, logarithmic behavior of λ sets in only at the latter stages after the surface becomes rough and the redeposition becomes significant.

In an attempt to elucidate the morphological evolution of the pre-rippled surface treated by CIBS, we conducted numerical studies with the KS equation. The input parameters were varied within the parameter space suggested by Makeev *et al.*[21] where ripple pattern is generated with its orientation parallel to the ion-beam direction, as observed in our experiment. We also examined the parameters predicted by both an SRIM simulation and our own MD simulation. However, we failed to reproduce the experimentally observed evolution of ripple patterns. Although the importance of the redeposition is indicated in previous discussions, a term $\nabla^2(\nabla h)^2$ that describes redeposition[23] is missing in the KS equation. Thus, the failure of the numerical simulation might be taken as an indirect evidence of the importance of the missing terms such as the redeposition.

V. SUMMARY AND CONCLUSION

We have reported the morphological evolution of a pre-rippled surface under crossing-ion-beam sputtering. In both the erosive and diffusive regimes, the amplitude of the pre-rippled surface decays exponentially with time when sputtered by an ion-beam crossing the initial ripple; new ripples develop along the direction of the crossing-ion beam only after the rippled surface becomes quite flat. Thus, a superimposed pattern of the initial and new ripple patterns is not observed, contrary to a recent theoretical prediction.[25]

With increasing ion fluence of the crossing-ion beam, the coarsening of the initial ripple follows a power law. The coarsening exponent n is 0.63 in the erosive regime and 0.74 in the diffusive regime. These values are much larger than those observed during the thermal coarsening of two-dimensional mounds, suggesting that different coarsening kinetics works for the initial ripples.

New ripples that form in the erosive regime show logarithmic coarsening. In contrast, for the initially flat surface, ripple coarsening shows a crossover from the power law to logarithmic behavior under the same sputtering conditions. The logarithmic behavior is attributed to enhanced redeposition for rough surface. A MD simulation of sputtering the pre-rippled surface also reveals that redeposition plays a significant role in its morphological evolution.

The BH and KS models cannot explain the observed morphological evolution of the pre-rippled surface such as the coarsening behavior. The hydrodynamic model self-consistently takes the redeposition effects into account and predicts the logarithmic coarsening of ripples.[23] This model is expected to help elucidate the present experimental results; such work is currently in progress.

ACKNOWLEDGMENTS

Comments from R. Cuerno and A. Enders are appreciated. The work is supported by KRF (Grant No. KRF-2007-314-C00078) and by NSF MRSEC (Grant No. DMR-0213808).

---

*jskim@sookmyung.ac.kr

[1] W. L. Chan and E. Chason, J. Appl. Phys. **101**, 121301 (2007).

[2] G. Carter and V. Vishnyakov, Phys. Rev. B **54**, 17647 (1996).

[3] J. Erlebacher, M. J. Aziz, E. Chason, M. B. Sinclair, and J. A. Floro, Phys. Rev. Lett. **82**, 2330 (1999).

[4] E. Chason, T. M. Mayer, B. K. Kellerman, D. T. McIlroy, and A. J. Howard, Phys. Rev. Lett. **72**, 3040 (1994).

[5] A. Toma, F. Buatier de Mongeot, R. Buzio, G. Firpo, S. R. Bhattacharyya, C. Boragno, and U. Valbusa, Nucl. Instrum. Methods Phys. Res. B **230**, 551 (2005).

[6] S. Habenicht, W. Bolse, K. P. Lieb, K. Reimann, and U. Geyer, Phys. Rev. B **60**, R2200 (1999).

[7] S. Rusponi, C. Boragno, and U. Valbusa, Phys. Rev. Lett. **78**, 2795 (1997).

[8] S. Rusponi, G. Costantini, C. Boragno, and U. Valbusa, Phys. Rev. Lett. **81**, 2735 (1998).

[9] W. L. Chan and E. Chason, Nucl. Instrum. Methods Phys. Res. B **242**, 228 (2006).

[10] Q. Wei, J. Lian, S. Zhu, W. Li, K. Sun, and L. Wang, Chem. Phys. Lett. **452**, 124 (2008).

[11] B. Ziberi, F. Frost, M. Tarts, H. Neumann, and B. Rauschenbach, Appl. Phys. Lett. **92**, 063102 (2008).

[12] S. Facsko, T. Dekorsy, C. Koerdt, C. Trappe, H. Kurz, A. Vogt, and H. L. Hartnagel, Science **285**, 1551 (1999).

[13] S. K. Mohanta, R. K. Soni, S. Tripathy, and S. J. Chua, Appl. Phys. Lett. **88**, 043101 (2006).

[14] T. C. Kim, C.-M. Ghim, H. J. Kim, D. H. Kim, D. Y. Noh, N. D. Kim, J. W. Chung, J. S. Yang, Y. J. Chang, T. W. Noh, B. Kahng, and J.-S. Kim, Phys. Rev. Lett. **92**, 246104 (2004).

[15] M. Lu, X. J. Yang, S. S. Perry, and J. W. Rabalais, Appl. Phys. Lett. **80**, 2096 (2002).

[16] R. M. Bradley and J. M. E. Harper, J. Vac. Sci. Technol. A **6**, 2390 (1988).

[17] P. Sigmund, Phys. Rev. **184**, 383 (1969).

[18] P. Sigmund, J. Mater. Sci. **8**, 1545 (1973).

[19] W. W. Mullins, J. Appl. Phys. **30**, 77 (1959).

[20] C. Herring, J. Appl. Phys. **21**, 301 (1950).

[21] M. A. Makeev, R. Cuerno, and A.-L. Barabasi, Nucl. Instrum. Methods Phys. Res. B **197**, 185 (2002).

[22] S. Facsko, T. Bobek, A. Stahl, H. Kurz, and T. Dekorsy, Phys. Rev. B **69**, 153412 (2004).

[23] J. Munoz-Garcia, M. Castro, and R. Cuerno, Phys. Rev. Lett. **96**, 086101 (2006).

[24] G. Carter, Vacuum **77**, 97 (2004).

[25] S. Vogel and S. J. Linz, Phys. Rev. B **75**, 085425 (2007).

[26] M. Joe, C. Choi, B. Kahng, and J.-S. Kim, Appl. Phys. Lett. **91**, 233115 (2007).

[27] U. Valbusa, C. Boragno, and F. B. de Mongeot, J. Phys.: Condens. Matter **14**, 8153 (2002).

[28] The morphological evolution by sputtering is affected by both the sputter erosion and by the diffusion of adatoms. Depending on the experimental condition, one of the two mechanisms may play a dominant role in the pattern formation. In the diffusive regime, where diffusion plays the major role, there form vacancy islands, upon sputtering at normal to the surface, because the adatoms diffuse so efficiently to the edge of the existing islands

and step edges. At grazing incidence, the adatoms generated by sputtering diffuse along the densely packed crystallographic directions in which the diffusion barriers for adatoms were relatively low and the resulting ripples are oriented along those directions irrespective of the sputter direction. In the erosive regime, sputter erosion plays the major role. Upon sputtering at normal to the surface, adatoms coalesce to form islands before they reach edges of the existing islands and step edges because the adatom density is so high and/or the diffusion is not that efficient. If the sputtering is made at grazing angle, the eroded surface is not effectively cured by diffusion of adatoms and the resulting ripples form by the sputter erosion along the sputtering direction. The diffusive regime is reached under sputtering conditions with low sputter yield or at low beam flux and ion energy and/or with the substrate at high temperature. The erosive regime is reached in the opposite conditions or high beam flux, ion energy, and/or low substrate temperature.

[29] A.-L. Barabási and H. E. Stanley, *Fractal Concepts in Surface Growth* (Cambridge University Press, Cambridge, England, 1995).

[30] The quality of fit is determined from reduced χ^2, which is defined by $\chi^2=\frac{1}{(n\text{-}p)}\sum_{i=1}^{n}\frac{(y_i-\hat{y}_i)^2}{\sigma_i^2}$, with y_i are experimental data points and $\hat{y}_i$ are obtained from a trial function, either a power-law, exponential, or logarithmic function. (n-p) describes degrees of freedom (DOF) where n being number of data points and p being number of parameters in the fitting function that is being used. Here, we use unweighted fitting where σ_i is set to be 1. The smaller χ^2 indicates the better fit.

[31] W. B. Fan, L. J. Qi, H. T. Sun, Y. Y. Zhao, and M. Lu, Nanotechnology **17**, 1878 (2006).

[32] W. B. Fan, L. Ling, L. J. Qi, W. Q. Li, H. T. Sun, C. X. Gu, Y. Y. Zhao, and M. Lu, J. Phys.: Condens. Matter **18**, 3367 (2006).

[33] N. Toyoda, T. Mashita, and I. Yamada, Nucl. Instrum. Methods Phys. Res. B **161-163**, 980 (2000).

[34] S. M. Foiles, M. I. Baskes, and M. S. Daw, Phys. Rev. B **33**, 7983 (1986).

[35] J. F. Ziegler, J. P. Biersack, and U. Littmark, *The Stopping and Range of Ions in Solids* (Pergamon, New York, 1985).

[36] M. A. Karolewski, Nucl. Instrum. Methods Phys. Res. B **230**, 402 (2005).

[37] J. D. Kress, D. E. Hanson, A. F. Voter, C. L. Liu, X.-Y. Liu, and D. G. Coronell, J. Vac. Sci. Technol. A **17**, 2819 (1999).

[38] I. M. Lifshitz and V. V. Slyozov, J. Phys. Chem. Solids **19**, 35 (1961).

[39] I. M. Lifshitz, Sov. Phys. JETP **12**, 939 (1962); S. M. Allen and J. W. Cahn, Acta Metall. **27**, 1085 (1979).

[40] K. Kern, I. K. Robinson, and E. Vlieg, Surf. Sci. **261**, 118 (1992).

[41] T. C. Kim, M. H. Jo, Y. Kim, D. Y. Noh, B. Kahng, and J.-S. Kim, Phys. Rev. B **73**, 125425 (2006).